A NEW MULTI-PHYSICS MOLECULAR DYNAMICS FINITE ELEMENT METHOD FOR DESIGNING GRAPHENE COMPOSITE NANO-STRUCTURES TO TARGET PROPERTY SPECIFICATIONS

A. A. R. Wilmes*[1], S. T. Pinho[1]

[1] *Department of Aeronautics, South Kensington Campus, Imperial College London. SW7 2AZ, UK.*
* *Corresponding Author: andre.wilmes07@imperial.ac.uk*

Keywords: MDFEM, Pillared Graphene Structures, Graphene Toughness, Multi-Physics

Abstract

A new multi-physics and multi-scale Molecular Dynamics Finite Element Method (MDFEM) is proposed, which allows for advanced mechanical and multi-physics charge-dipole MD force fields to be implemented exactly in the computationally more favourable FEM. The proposed model has produced novel mechanical and electrical charge-dipole FEM results. In particular the homogenised mechanical in-plane and bending properties of Pillared Graphene Structures (PGS) as well as the fracture toughness properties of pristine graphene have been obtained. The presented MDFEM is well suited for the optimised virtual design of a wide range of electro-mechanical nano-devices or nano-structures, e.g. PGS, to either given device property or macroscopic target specifications.

1. Introduction

Emerging 2D materials such as graphene or boron-nitride have led to the synthesis of novel 3D-layered systems. These engineered materials represent the advent of a new class of composites, with atomic structures controllably designed at the nano-scale, which potentially offer unprecedented properties and functionalities for a wide range of engineering applications [1].

Scalable manufacturing processes, e.g. Roll-to-Roll Chemical Vapour Deposition and Nanoimprint Lithography, allow for the meter-scale synthesis of bulk nano-material with engineered nanometer sized features. Novel graphene based material nano-structures such as 3D Pillared Graphene (PGS) [2] hold a high transformative potential for nano-layer reinforced structural composites. PGS are predicted to have outstanding 3D mechanical properties [3], while lithium-doped PGS are expected to have unique hydrogen storage capacities above 6 wt % [4], due to the alkali ion's charge-induced dipoles in the H_2; potentially offering the first commercially viable material for H_2-fuelled mobile applications, e.g. cars, phones.

This nano-manufacturing progress creates a new need for corresponding physically accurate and numerically efficient modelling methods. Modelling large atomic structures is unaffordable with Quantum Mechanics (QM) or even Molecular Dynamics (MD). Computationally affordable continuum based methods, e.g. Finite Element Method (FEM), inherently struggle to capture important discrete physical features, e.g. lattice defects governing critical fracture.

The MD method has increasingly been incorporated in FEM [5–9] for structural simulations, as the equilibrium equations of MD and FEM can be expressed in equivalent forms. The resulting MDFEM is computationally more favourable than MD [6], while offering increased compatibility for multi-scale simulations with larger scale continuum FEM.

Readily available, structural mechanics FEM elements (e.g. beams) have been used for MDFEM [8, 9]. However, their use is detrimental to MDFEM's full mechanical non-linear capabilities and prohibits all multi-physics. Several MDFEM proposed mechanically non-linear elements [5–7, 10] with varying complexity and flexibility in accommodating different MD force fields; yet a general MDFEM including multi-physics has not been proposed.

This paper derives a new MDFEM [11], embedding the equilibrium equations of MD within the computationally more favourable FEM, in order to model complex 3D nano-structures across generic load cases with simple element topologies and full multi-physics force field flexibility.

The key novel aspects of the proposed model, which represent new contributions to the state of the art, are: (i) a mathematically robust multi-physics derivation; (ii) the formal separation of force field and element topology information; (iii) the differentiation between constitutive, geometrical and mixed instabilities; (iv) a mathematically and numerically optimised, symbolic processor based, implementation; (v) both explicit and implicit FEM formulations, where the latter allows for large time and spacial scales, eigenvalue analyses, and a singular mass matrix; (vi) local/non-local periodic boundary conditions under torsion/bending deformations.

The proposed multi-physics and multi-scale compatible MDFEM is equivalent to MD, as shown by the analyses of brittle fracture in Carbon Nanotubes (CNT) with defects, but at a considerably reduced computational cost. Electro-mechanical examples of electric field induced polarisations in CNT and charge distribution in graphene as well as examples of concurrently coupled MD and continuum FEM domains demonstrate the MDFEM to be well suited for both multi-scale and multi-physics modelling. Homogenised mechanical properties for PGS are obtained, which allows the MDFEM to design graphene nano-structures to target property specifications in a parametric study approach. Finally, by eigenvalue-based modelling of buckling, failure, vibrational, piezoelectric and electric-field induced polarisation behaviours, among others, this method can contribute to the design of nano-scale graphene composites, sensors, H_2 storage and other multi-functional nano-materials.

2. Multi-Physics Equilibrium, Hamilton Principle and a Discrete Finite Element Method

Hamilton's Principle is a formal and natural approach to describe equilibrium in a discrete multi-physics system and can lead to Lagrange's equation by a Legendre Transform:

$$\frac{\mathrm{d}}{\mathrm{d}t}\left(\frac{\partial\left(T^*(\dot{\mathbf{q}})\right)}{\partial\dot{\mathbf{q}}}\right)^{\mathrm{T}}+\left(\frac{\partial\left(V(\mathbf{q})\right)}{\partial\mathbf{q}}\right)^{\mathrm{T}}=\mathbf{f}\,, \tag{1}$$

where the system's n generalised displacements are denoted by $\mathbf{q}\in\mathbb{R}^{n\times1}$, the corresponding generalised forces by $\mathbf{f}\in\mathbb{R}^{n\times1}$ and the multi-physics conservative generalised potential energy by V. The system's generalised kinetic co-energy is assumed to be dependent on the generalised velocities only, i.e. $T^*=T^*(\dot{\mathbf{q}})$, and is formally defined as $T^*\triangleq\int\mathbf{p}\,\mathrm{d}\dot{\mathbf{q}}=T^*(\dot{\mathbf{q}})$, where $\mathbf{p}\in\mathbb{R}^{n\times1}$ represents the generalised momenta. Finally, t denotes time.

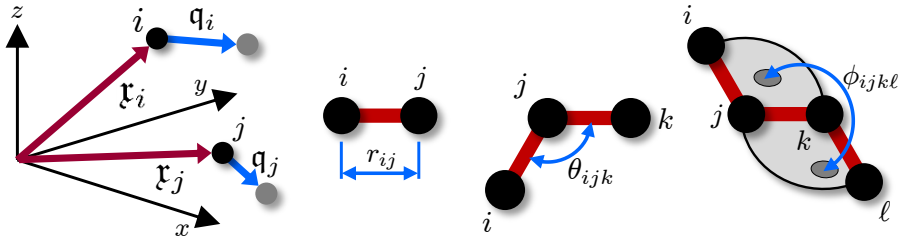

Figure 1: Generalised displacements for atoms i and j and selected MD characteristic variables.

The set of displacements, $\mathbf{u}$, partial electric charges, $\mathbf{q}$, and electric dipoles, $\mathbf{p}$, of all atoms constitute an comprehensive and natural choice of $\mathfrak{q}$ for a discrete particle system, see Fig. 1. Hence, the corresponding generalised forces, $\mathfrak{f}$, are a set of mechanical forces, $\mathbf{f}$, point electric potentials, $\boldsymbol{\phi}$, and point electric field values, $\mathbf{E}$. Lagrange's equation, Eq. (1), thus becomes:

$$\mathbf{M}(\dot{\mathfrak{q}})\,\ddot{\mathfrak{q}} + \left(\mathbf{J}_{\mathfrak{q}}^{V}\right)^{\mathrm{T}} = \mathfrak{f}\,, \quad \text{while defining} \quad \mathbf{J}_{\mathfrak{q}}^{V} = \frac{\partial V(\mathfrak{q})}{\partial \mathfrak{q}} \quad \text{and} \quad \mathbf{H}_{\mathfrak{q}}^{V} = \frac{\partial}{\partial \mathfrak{q}}\left(\frac{\partial V(\mathfrak{q})}{\partial \mathfrak{q}^{\mathrm{T}}}\right), \tag{2}$$

as the potential energy's Jacobian and Hessian relative to the displacements respectively. The generalised mass matrix, $\mathbf{M}(\dot{\mathfrak{q}})$, may be singular for physics with non-defined momenta or non-constant for physics with non-linear momenta-velocity relations. Eq. (2) suggests an analogy with FEM and can be solved using a Hessian-based Newton-Raphson scheme.

3. MDFEM with Constitutive Relations Uncoupled from Geometric Element Topologies

The MD potential energy, V, generally consists of superposed partitioned sub-potentials, V_S :

$$V(\mathbf{c}) = \sum_{\mathbb{S}} V_S(\mathbf{c}_S) = \sum_{\mathbb{S}} \sum_{i=1}^{n_p^S} V_S^i\left(\mathbf{c}_S^i\left(\mathfrak{x}_S^i, \mathfrak{q}_S^i\right)\right), \tag{3}$$

where $\mathbf{c}$ represents the potential's characteristic variables (e.g. bond lengths/angles). Each sub-potential (e.g. stretch energy) is further divided into partitions (e.g. bonds). Classical force fields include sub-potentials for mechanical deformation modes (e.g. bond stretching, torsion, stretch-bend), while the charge-dipole potentials [12], cause electro-mechanical couplings.

The smallest element topology representing one partition, $V_S^i\left(\mathbf{c}_S^i\left(\mathfrak{x}_S^i, \mathfrak{q}_S^i\right)\right)$, is identical to the latter's characteristic variable-defining sketch, see Fig. 1. The elements are superposed during meshing and the system's overall Jacobian, $\mathbf{J}_{\mathfrak{q}}^{V}$ and Hessian, $\mathbf{H}_{\mathfrak{q}}^{V}$ in Eq. (2) are obtained by an FEM-typical assembly of the elements' Jacobian, $\mathbf{J}_{\mathfrak{q}_S^i}^{V_S^i}$, and Hessian, $\mathbf{H}_{\mathfrak{q}_S^i}^{V_S^i}$, which are obtained as:

$$\mathbf{J}_{\mathfrak{q}_S}^{V_S} = \mathbf{J}_{\mathbf{c}_S}^{V_S}\mathbf{J}_{\mathfrak{q}_S}^{\mathbf{c}_S}\,, \quad \text{and} \quad \mathbf{H}_{\mathfrak{q}_S}^{V_S} = \left(\mathbf{J}_{\mathfrak{q}_S}^{\mathbf{c}_S}\right)^{\mathrm{T}}\mathbf{H}_{\mathbf{c}_S}^{V_S}\mathbf{J}_{\mathfrak{q}_S}^{\mathbf{c}_S} + \sum_{k=1}\left(\mathbf{J}_{\mathbf{c}_S}^{V_S}\right)_k \mathbf{H}_{\mathfrak{q}_S}^{c_{S_k}}\,, \tag{4}$$

where the i indeces were omitted, the $\mathbf{J}_{\mathbf{c}_S}^{V_S}$ and $\mathbf{H}_{\mathbf{c}_S}^{V_S}$ refer to the *Potential Jacobian* and *Potential Hessian*. Similarly, $\mathbf{J}_{\mathfrak{q}_S}^{\mathbf{c}_S}$ and $\mathbf{H}_{\mathfrak{q}_S}^{\mathbf{c}_S}$ denote the *Geometric Jacobian* and *Geometric Hessian*.

The *Reconstruction Equations*, Eq. (4), lead to the following advantages:
(i) *Separation of Force Field Potentials from Element Topologies*; (ii) *Reduced Complexity of Derivatives*; (iii) *Independent Scaling of Derivatives' Length*; (iv) *Enhanced Computational Performance*; (v) *Independent Analysis of Geometrical, Constitutive and Mixed Instabilities*.

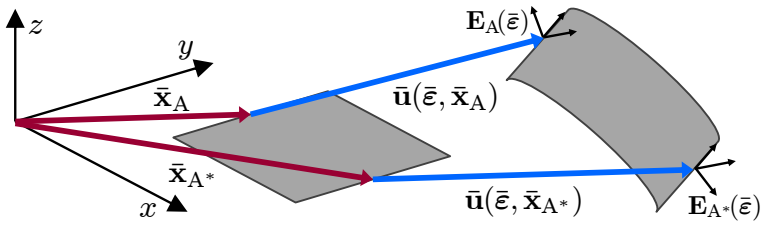

Figure 2: A 2D Unit Cell in an undeformed and homogeneous deformed state

4. Local & Non-Local PBC for Low-Dimensional Unit Cells with Rotations

PBC for low-dimensional molecular UC domains present two challenges: (i) the periodic deformation fields may include bending/rotations; (ii) the non-locality of the molecular force field expressions requires the computation of mirror atoms' positions inside adjacent unit cells.

Considering Fig. 2, any periodic molecular UC may be placed inside a simulation space domain of appropriate dimensionality, which deforms according to some kinematic relations $\bar{\mathbf{r}} = \bar{\mathbf{x}} + \bar{\mathbf{u}}(\bar{\boldsymbol{\varepsilon}}, \bar{\mathbf{x}})$. During deformation, which includes micro-fields, the periodicity of the internal atomic structure must be maintained relative to the local coordinate systems $\mathbf{E}_{\mathrm{A}}$ and $\mathbf{E}_{\mathrm{A}^*}$ associated with equivalent points such as A and A^*. Hence the local boundary PBC may be stated as:

$$\left(\mathbf{r}_{i^*} - \bar{\mathbf{r}}\left(\bar{\boldsymbol{\varepsilon}}, \bar{\mathbf{x}}_{\mathrm{A}^*}\right)\right) = \mathbf{R}_{\mathrm{AA}^*}(\bar{\boldsymbol{\varepsilon}}) \left(\mathbf{r}_i - \bar{\mathbf{r}}\left(\bar{\boldsymbol{\varepsilon}}, \bar{\mathbf{x}}_{\mathrm{A}}\right)\right) , \tag{5}$$

for equivalent atoms i and i^* on the boundary. $\mathbf{R}_{\mathrm{AA}^*}(\bar{\boldsymbol{\varepsilon}})$ denotes a real unitary, rotational matrix which is obtained as $\mathbf{R}_{\mathrm{AA}^*} = \mathbf{E}_{\mathrm{A}}\, \mathbf{E}_{\mathrm{A}^*}^{-1}$. $\mathbf{E}$ is deducible from $\bar{\mathbf{r}}\,(\bar{\boldsymbol{\varepsilon}})$, and for a plate, two tangential unit vectors and the normal constitute a natural choice. Similarly, an atom $i_{(n)}$, corresponding to atom i but n cells away in the x-direction in Fig. 2, may be mapped as:

$$\mathbf{r}_{i(n)} = \bar{\mathbf{r}}\left(\bar{\boldsymbol{\varepsilon}}, \bar{\mathbf{x}}_{\mathrm{A}}\right) + \sum_{j=0}^{n} \left[\mathbf{R}_{\mathrm{AA}^*}^{j} \left(\bar{\mathbf{r}}\left(\bar{\boldsymbol{\varepsilon}}, \bar{\mathbf{x}}_{\mathrm{A}^*}\right) - \bar{\mathbf{r}}\left(\bar{\boldsymbol{\varepsilon}}, \bar{\mathbf{x}}_{\mathrm{A}}\right)\right)\right] + \mathbf{R}_{\mathrm{AA}^*}^{n} \left(\mathbf{r}_i - \bar{\mathbf{r}}\left(\bar{\boldsymbol{\varepsilon}}, \bar{\mathbf{x}}_{\mathrm{A}^*}\right)\right) . \tag{6}$$

Finally, if the kinematic variables $\bar{\boldsymbol{\varepsilon}}$ are free DoF, and the kinematic relations $\bar{\mathbf{u}}$ respect a structural theory, e.g. plate theory, homogenised properties may be obtained easily.

5. Implementation

The presented formulation was implemented symbolically in MATLAB[1]. A *Force Field Library* contains a range of MD force fields while an *Element Library* stores all available characteristic variable definitions. Using these libraries, the requested geometry is generated and meshed with all required elements before the tensors $\mathbf{J}_{\mathbf{c}_S}^{V_S}$, $\mathbf{J}_{\mathbf{q}_S}^{\mathbf{c}_S}$, $\mathbf{H}_{\mathbf{c}_S}^{V_S}$ and $\mathbf{H}_{\mathbf{q}_S}^{\mathbf{c}_S}$ are symbolically derived[2]. The resultant algebraic expression are exported in a numerically optimised FORTRAN-90/95 format, which is suitable for the implicit and explicit FE package ABAQUS[3].

[1] MATLAB R2012a, The MathWorks Inc.

[2] The software corresponding to this model's implementation will be made available at: www.imperial.ac.uk/people/silvestre.pinho

[3] ABAQUS 6.12-1, Dassault Systemes Simulia Corp.

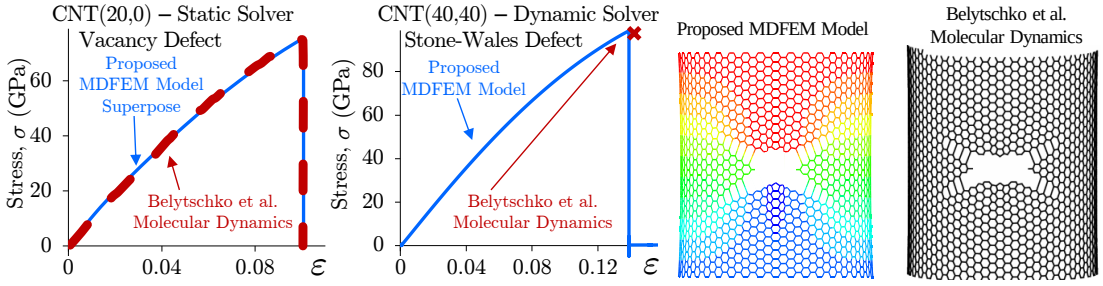

Figure 3: The proposed MDFEM gives constitutive responses equivalent to full MD [13], including failure, crack initiation and propagation for CNT of varying chirality with defects.

6. Applications

6.1. Brittle Failure of Carbon Nanotubes with Defects & Linear Computational Scaling

The MD study by Belytschko et al. [13], a mechanical MD study (i.e. $\mathbf{q} = \mathbf{u}$ and $\mathbf{f} = \mathbf{f}$), on the effects of vacancy, Stone-Wales and weakened-bond defects on the constitutive fracture responses of CNT was chosen to demonstrate the equivalence of the proposed MDFEM and MD in a highly non-linear environment in both static and dynamic implicit FE analyses. Following Belytschko et al. [13], the original bond-order potential is approximated by a Morse potential:

$$V = V_S + V_B = \alpha \left\{ \left[1 - e^{-\beta(r_{ij}-r_0)} \right]^2 - 1 \right\} + \frac{1}{2}\gamma \left(\theta_{ijk} - \theta_0\right)^2 \left[1 + \lambda \left(\theta_{ijk} - \theta_0\right)^4 \right], \qquad (7)$$

with $r_0 = 1.39$ Å, $\theta_0 = 2.094$ rad, $\alpha = 6.03105$ nN Å, $\beta = 2.625$ Å^{-1}, $\gamma = 9.0$ nN Å rad^{-2} and $\lambda = 0.754$ rad^{-4}. The conventional stress-strain responses assume a wall thickness of $t_{\text{wall}} = 3.4$ Å.

The constitutive response of a CNT$(20, 0)$ with a vacancy defect, Fig. 3, obtained by a static implicit analysis, is in excellent agreement with MD [13]; similarly to the three other CNT configurations with different defect types each. These static simulation only took $\mathcal{O}\left(10^1 - 10^2\right)$ seconds of CPU time on a standard workstation with 3.3 GHz Intel i5-2500 processors.

For a CNT$(40, 40)$ with a Stone-Wales defect, a failure strain and stress of 13.9 % and 98.8 GPa were obtained by a dynamic implicit analysis, which compare well with the reference MD results of 14.2 % and 97.5 GPa, see Fig. 3. Moreover, the implicit dynamic solver is able to compute converged dynamic equilibrium points at the onset of, and during fracture.

The numerical performance of the proposed model was tested by stretching CNT$(5, 5)$ to 5 % strain. Continuously larger nanotubes with up to 1.0 million atoms, with a length of 12 μm, were run on the same workstation, showing the static implicit formulation to scale linearly, Fig. 4.

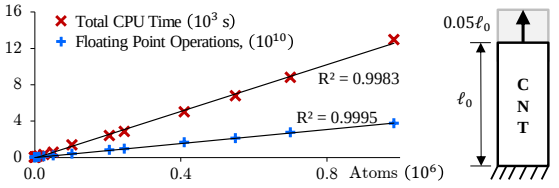

Figure 4: MDFEM has linear computational scaling.

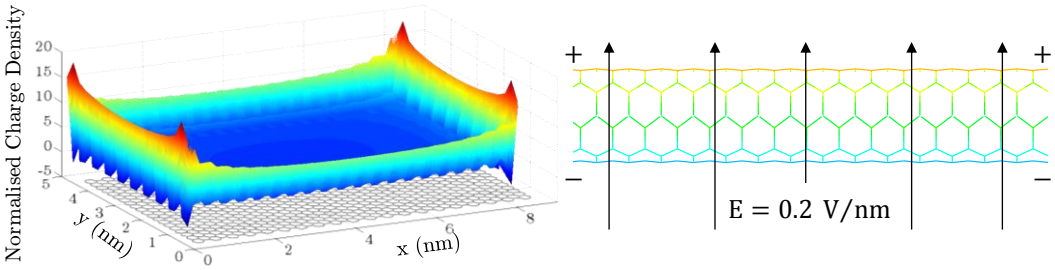

Figure 5: Interpolated normalised charge density for a charged 8.5 nm × 4.8 nm graphene sheet and a cut-view of the electric-field induced charge polarisation in a neutral, insulated CNT.

6.2. Charge Densities & Electric Field Induced Polarisations

Various reported electro-mechanical effects including, charge induced mechanical strains in CNT up to failure, charge distributions in CNT deposited on substrates, pseudo-magnetic fields, electric field induced deflections and vibrations of graphene and CNT, can now be modelled within FEM to design electro-mechanical nano-systems.

The distribution in a charged graphene sheet, Fig. 5, was obtained using the anisotropic-polarisation charge-dipole force field Q+P aniso [12], together with the AIREBO potential. Charge accumulates along the edges and corners, reaching normalised charge densities (relative to the charge at the centre) of 7 and 15 respectively, which agrees with literature [14].

Fig. 5 shows a CNT subjected to a perpendicular electric field. A charge separation in the neutral CNT is induced, causing an overall polarisation. If perturbed away from the perpendicular alignment of the electric field, axially-aligned induced dipoles can spark an electric-field driven buckling behaviour of the CNT, which may be used to design detectors and switches.

6.3. Eigenvalue Analyses & Multi-Scale MD and FEM Domains

The implicit formulation's eigenvalue analyses can determine vibrational frequencies of molecular devices, such as simply or doubly-clamped CNT, Fig. 6. Experimental results for electric-field induced vibrational frequencies of simply-clamped CNT have been reported [15], and as shown above, CNT with length-scales in the micrometre range can easily be modelled.

Equally, the proposed model is well suited for hierarchical or concurrent multiscale coupling with continuum FEM, Fig. 6, allowing for further computational savings with MDFEM also avoiding the need for coupling separate numerical solvers.

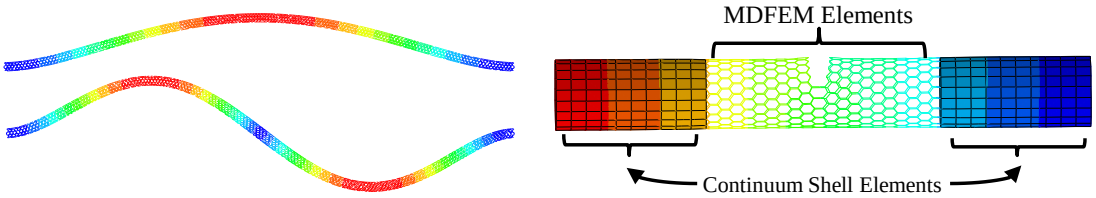

Figure 6: First two mechanical vibration mode shapes of a doubly-clamped CNT and a concurrent continuum FEM & MD simulation of a CNT with a defect during failure onset.

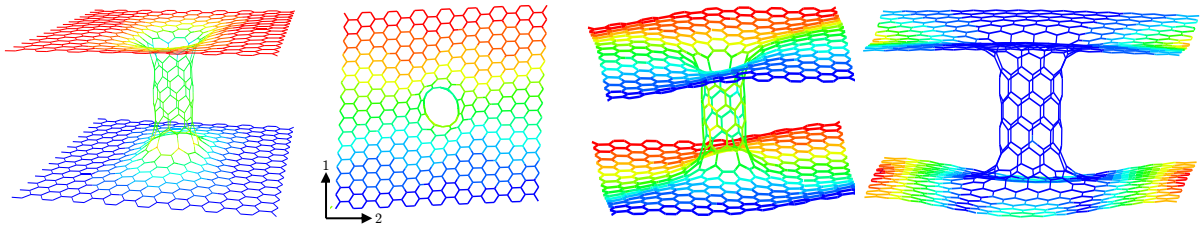

Figure 7: An undeformed PGS Unit Cell is subjected to pure shear (top/side-view) and bending.

6.4. Homogenised Properties of Graphene and 3D Pillared Graphene Structures

Using the Lobo-Keating potential, [16], both a graphene (G) unit cell and a PGS unit cell was subjected to rotational PBC, which were based on classical Kirchoff plate strain kinematics, e.g. in-plane, pure shear, bending and twist deformations. The homogenised properties are reported as the typical **A** [TPa-nm] and **D** [TPa-nm^3] matrices of plate theory, as to avoid ambiguities with the thickness and continuum assumptions.

	A_{11}	A_{12}	A_{22}	A_{33}	D_{11}	D_{12}	D_{22}	D_{33}
G	0.2242	0.0182	0.2242	0.4044	0.1294×10^{-3}	-	0.1294×10^{-3}	N/A
PGS	0.3392	0.0731	0.3905	0.6409	0.0618	0.1654	0.0735	0.0680

Table 1: Homogenised Mechanical In-Plane & Bending Properties of Graphene and PGS

While the PGS's and graphene's in-plane stiffness (**A**) is of the same order of magnitude, the bending properties (**D**) of the PGS are more than two orders of magnitude higher than those of graphene. No twist rigidity is presented for graphene as the force field does is not applicable for linear twist. Fig. 7 shows that during pure shear as well as bending, the initial small in-plane waviness of the PGS is amplified. Lithium-doped PGS are predicted to possess unrivalled H_2 storage capacities at ambient conditions [4]. Hence, the proposed model, with its ability to incorporate both advanced mechanical as well as polarisable charge-dipole force fields, is ideally suited to perform parametric topology studies of the homogenised electro-mechanical, fracture and H_2 storage properties of such hybrid PGS.

6.5. Stress Intensity Factor & Toughness of Macro-Sized Graphene

The proposed model's computational scaling allows for modelling graphene sheets with 1-2 million atoms and thus maco-sized dimensions up to 200 nm. This enables to determine the fracture toughness of graphene in both the zig-zag and armchair direction. Fracture toughness values, obtained using a crack compliance approach, will be presented at the conference.

7. Conclusion

A new MDFEM has been formally derived from first principles and implemented; with a key novelty being the formal separation of *potential* and *geometric* relations which permits combining different force fields and element topologies, analogously to the separation of element types and constitutive laws in FEM.

The proposed model: (i) has been shown to be exactly equivalent to MD; (ii) has produced novel mechanical and charge-dipole FEM results; (iii) allows for low-dimensional UC kinematics under novel torsional PBC; (iv) does not require artificial kinetic co-energies of energy forms with no physical momenta (i.e allowing a singular generalised mass matrix **M**) (v) is computationally more favourable than MD with a linear numerical scaling; (vi) offers a broader range of analyses techniques over wider length and time scales; (vii) is inherently well-suited for multi-scale; (viii) is applicable to any chemical structure with any number of species; (ix) is applicable for both zero and finite temperatures.

The proposed model represents a unified formulation of MD bridging from small to large time and spacial scales, as well as across different physics, while inherently offering convenient multi-scale integration with continuum FEM domains. Hence it will allow for the optimised virtual design of a wide range of electro-mechanical nano-devices and nano-structures to either given device property or macroscopic target specifications; which may include the piezoelectric property couplings in CNT or PGS during vibrations; H_2 storage in PGS; and homogenised properties for different homo- and heteroatomic nano-structures to be used in industrial applications such as structural composites, coatings and flexible electronics.

References

[1] M.J. Allen, V.C. Tung, and R.B. Kaner. Honeycomb carbon: a review of graphene. *Chem.Rev.*, 110:132, 2010.

[2] K. Spyrou, L. Kang, E.K. Diamant, R.Y. Gengler, D. Gournis, M. Prato, and P. Rudolf. A novel route towards high quality fullerene-pillared graphene. *Carbon*, accepted 2013.

[3] L. Xu, N. Wei, Y. Zheng, Z. Fan, H.Q. Wang, and J.C. Zheng. Graphene-nanotube 3d networks: intriguing thermal and mechanical properties. *J. Mater. Chem.*, 22:1435–1444, 2012.

[4] G.K. Dimitrakakis, E. Tylianakis, and G.E. Froudakis. Pillared graphene: A new 3-d network nanostructure for enhanced hydrogen storage. *Nano Letters*, 8:3166–3170, 2008.

[5] Y. Wang, C. Sun, X. Sun, J. Hinkley, G.M. Odegard, and T.S. Gates. 2-d nano-scale finite element analysis of a polymer field. *Compos.Sci.Technol.*, 63:1581–1590, 2003.

[6] B. Liu, Y. Huang, H. Jiang, S. Qu, and K.C. Hwang. The atomic-scale finite element method. *Comput.Method.App.M.*, 193:1849–1864, 2004.

[7] T.C. Theodosiou and D.A. Saravanos. Numerical simulations using a molecular mechanics-based finite element approach: application on boron nitride armchair nanotubes. *(Int.J.Comput.Meth.Eng.Sci.Mech.*, 12:203–211, 2011.

[8] G.M. Odegard, T.S. Gates, L.M. Nicholson, and K.E. Wise. Equivalent-continuum modeling of nano-structured materials. *Compos.Sci.Technol.*, 62:1869–1880, 2002.

[9] X. Sun and W. Zhao. Prediction of stiffness and strength of single-walled carbon nanotubes by molecular-mechanics based finite element approach. *Mat.Sci.Eng.A-Struct.*, 390:366–371, 2005.

[10] J. Wackerfuß. Molecular mechanics in the context of the finite element method. *Int.J.Numer.Meth.Eng.*, 77:969–997, 2009.

[11] A.A.R. Wilmes and S.T. Pinho. A new molecular dynamics finite element method with multi-scale and multi-physics applications to failure of graphene structures. In Submission 2013.

[12] A. Mayer. Formulation in terms of normalized propagators of a charge-dipole model enabling the calculation of the polarization properties of fullerenes and carbon nanotubes. *Phys.Rev.B*, 75:045407, 2007.

[13] T. Belytschko, S.P. Xiao, G.C. Schatz, and R.S. Ruoff. Atomistic simulations of nanotube fracture. *Phys.Rev.B*, 65:235430, 2002.

[14] Z. Wang and R.W. Scharstein. Electrostatics of graphene: charge distribution and capacitance. *Chemical Physics Letters*, 489:229–236, 2010.

[15] P. Poncharal, Z.L. Wang, D. Ugarte, and W.A. de Heer. Electrostatic deflections and electromechanical resonances of carbon nanotubes. *Science*, 283:1513–1516, 1999.

[16] C. Lobo and J.L. Martins. Valence force field model for graphene and fullerenes. *Z.Phys.D.Atom.*, 39:159–164, 1997.